Frontiers in Batteries and Electrochemistry

TYPE Original Research
PUBLISHED 01 May 2024
DOI 10.3389/fbael.2024.1388494

OPEN ACCESS

EDITED BY
Wei Tong,
Berkeley Lab (DOE), United States

REVIEWED BY
Dewei Wang,
North Minzu University, China
Bapi Bera,
University of Tennessee, Knoxville,
United States

*CORRESPONDENCE
Hongmei Luo,
hluo@nmsu.edu

[†]These authors have contributed equally to this work

RECEIVED 19 February 2024
ACCEPTED 15 April 2024
PUBLISHED 01 May 2024

CITATION
Truong P, Sun Q, Tang W, He R, Zhou M and Luo H (2024), Morphology modification of $LiNi_{0.5}Co_{0.2}Mn_{0.3}O_2$ by incorporating cotton textiles in lithium-ion capacitors.
Front. Batteries Electrochem. 3:1388494.
doi: 10.3389/fbael.2024.1388494

Morphology modification of $LiNi_{0.5}Co_{0.2}Mn_{0.3}O_2$ by incorporating cotton textiles in lithium-ion capacitors

Phat Truong[†], Quanwen Sun[†], Wei Tang, Rong He, Meng Zhou and Hongmei Luo*

Department of Chemical and Materials Engineering, New Mexico State University, Las Cruces, NM, United States

To address the alerting issue of energy demand, lithium-ion capacitors (LICs) have been widely studied as promising electrochemical energy storage devices, which can deliver higher energy density than supercapacitors (SCs), and have higher power density with longer cycling life than lithium-ion batteries (LIBs). In this work, the active material lithium nickel cobalt manganese oxide $LiNi_{0.5}Co_{0.2}Mn_{0.3}O_2$ (NCM523) is grown on a cotton textile template and building a 3-dimensional (3D) integrity to improve capacitance and energy density of LICs by enhancing the interfacial ion-exchange process. With the 3D structure, the specific discharge capacitance is increased to 718.67 $F\,g^{-1}$ at 0.1 $A\,g^{-1}$ from that of non-textile NCM523 (265.97 $F\,g^{-1}$), and remains a high capacitance of 254.48 Fg^{-1} at 10 $A\,g^{-1}$ in the half-cell capacitors. In addition, the energy density can achieve up to 36.17 $Wh\,kg^{-1}$ at the power density of 1,200 $W\,kg^{-1}$ in the full-cell capacitor. The textile NCM can maintain an energy density of 28.26 $Wh\,kg^{-1}$ at the current density of 10 $A\,g^{-1}$ and power density of 6,000 $W\,kg^{-1}$. Our results present promising applications of electrodes with the 3D porous structure for high energy density LICs.

KEYWORDS

lithium-ion capacitor (LIC), 3D structure, lithium nickel cobalt manganese oxide (NCM), energy density, battery cathode material

1 Introduction

The consumption and the demand for conventional energies are increasing along with the alerting issue of greenhouse gas emissions (Su et al., 2015; Yuan et al., 2016; Supply, 2021). In response, different energy storage devices have been developed to store and utilize clean renewable energies (engineering, 2017). However, such devices remain inferior to the ideal performance of the traditional combustion engine (Gnanomat, 2019). Taking supercapacitors (SCs) as an example, they are recognized with high power density yet compromised energy density (Education, 2018; Sedajová et al., 2020). Instead, lithium-ion capacitors (LICs) are considered as promising electrochemical energy storage devices, which can deliver higher energy density than SCs and have higher power density with longer cycling life than lithium-ion batteries (LIBs).

The theory is proposed based on the charge-storage mechanism of LIB and SC. Specifically, when a battery is discharged, lithium ions are released from the anode and intercalate into the vacant sites at the cathode's lattice structure (Lee and Im, 2018). Despite

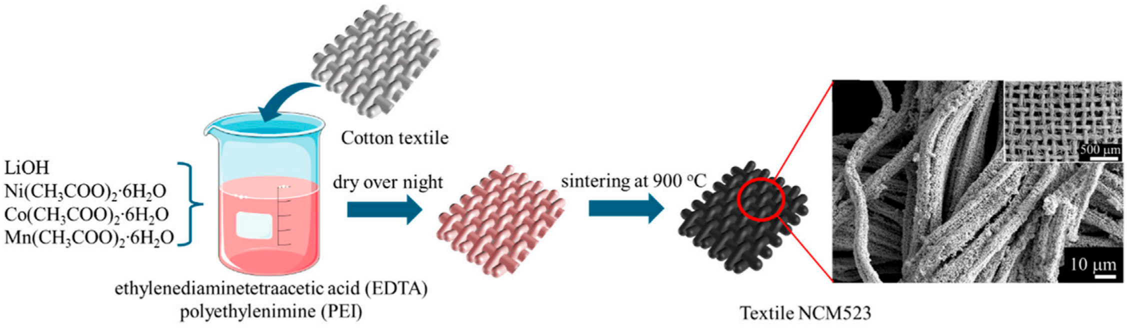

FIGURE 1
The synthesis process of 3D structure of NCM523.

the sluggish intercalation process, it allows LIBs to reach higher energy density (Vlad et al., 2014). On the contrary, SCs have high power density thanks to their rapid charge-discharge process, but the electrochemical reactions only occur on the electrode's surface causing low energy density (Kötz and Carlen, 2000; Lewandowski and Galinski, 2007; Sharma and Bhatti, 2010). As a result, hybridizing the LIB's cathode active materials (CAMs) with SC's electrochemical double-layered capacitor (EDLC) component is expected to render a synergistic effect to control both the energy and power densities, (Vlad et al., 2014; Hagen et al., 2018; Zhao et al., 2020), which is named LICs. Up to now, there have been some promising progress reported. For instance, an energy density of more than 3 times that a conventional supercapacitor can reach has been achieved by employing $Li_4Ti_5O_{12}$ (LTO) with graphite (Amatucci et al., 2001; Chen et al., 2012). However, the hybridization remains under-optimized due to the low power characteristic caused by poor Li^+ diffusion coefficient and poor electronic conductivity (Kuwata et al., 2016). In response, with the incorporation of textiles to build a 3D skeleton, the problems of Li^+ diffusion and ion exchange are substantially mitigated through increased porosity and surface area.

In this work, to further enhance their electrochemical performances of capacitance and energy density, $LiNi_{0.5}Co_{0.2}Mn_{0.3}O_2$ (NCM523) was incorporated with cotton textiles during the synthesis process to construct a 3D integrity. The NCM523 is selected to inherit the good cycle performance and to avoid cation mixing in Ni-rich NCM materials, while the incorporation of textiles during the synthesis process would expedite the interfacial ion-exchange processes to improve the energy density (Muto et al., 2009; Zhao et al., 2020; Zhao and Li, 2020). From which, a new record of energy density (28.26 Wh kg^{-1}) has been written while maintaining the same level of power density (6,000 W kg^{-1}) at a high current rate of 10 A g^{-1}.

2 Experimental section

2.1 Preparation of NCM523

The polymer solution was prepared by mixing ethylenediaminetetraacetic acid (EDTA) and polyethylenimine (PEI, 50% in water) under a ratio of 1:2 in 20 mL of deionized (DI) water. Then, LiOH, Ni $(CH_3COO)_2{\cdot}6H_2O$, Co $(CH_3COO)_2{\cdot}6H_2O$, and Mn $(CH_3COO)_2{\cdot}6H_2O$ (1.5:0.5:0.2:0.3) were added into the polymer solution once it reached homogeneity. 50% excess of lithium was applied to account for its evaporation during the high-temperature annealing process. Cotton textiles were soaked in the solution as templates for 3D NCM523 synthesis, and the mixture was kept stirring at 80℃ overnight until a highly viscous gel was obtained. After that, the gel with the textiles was transferred to a muffle furnace to calcine at 500℃ for 5 h and 900℃ for 10 h at a ramp rate of 1℃ min^{-1}. The synthesis process of 3D structure of NCM523 is shown in Figure 1. For comparison, a control sample of NCM523 without textile (non-textile NCM523) was prepared under the same conditions.

2.2 Characterizations

Thermo-gravimetric analysis (TGA—Thermogravimetric Analyzer Model 500 from the TA Instrument) was conducted to find the appropriate annealing temperature. The material morphology and phase structure were analyzed using Scanning Electron Microscope (SEM—Hitachi Model S-3400N II) and X-ray diffraction (XRD—Empyrean XRD PANalytical). The surface area and composition of elements in electrode material were examined by Brunauer–Emmett–Teller (BET—Micromeritics ASAP 2050 High-Pressure Sorption Analyzer) and Inductively Coupled Plasma (ICP—Octopole Reaction System (ORS) Agilent 7500ce with a CETAC XS520 autosampler).

2.3 Electrochemical measurements

Ni-foams were pre-treated with HCl and washed with ethanol and acetone, which were dried at 80℃ in a vacuum oven. The slurry was made by grinding the NCM523 (80 wt%) with carbon black super-P (CB-super P) (10 wt%) and polyvinylidene fluoride (PVDF) (10 wt%) then adding drop-wise N-methyl-2-pyrrolidone (NMP) until honey-like viscosity was obtained. The electrode was prepared by loading the slurry onto the Ni-foams and dried in a vacuum oven overnight. The mass loading was maintained at around

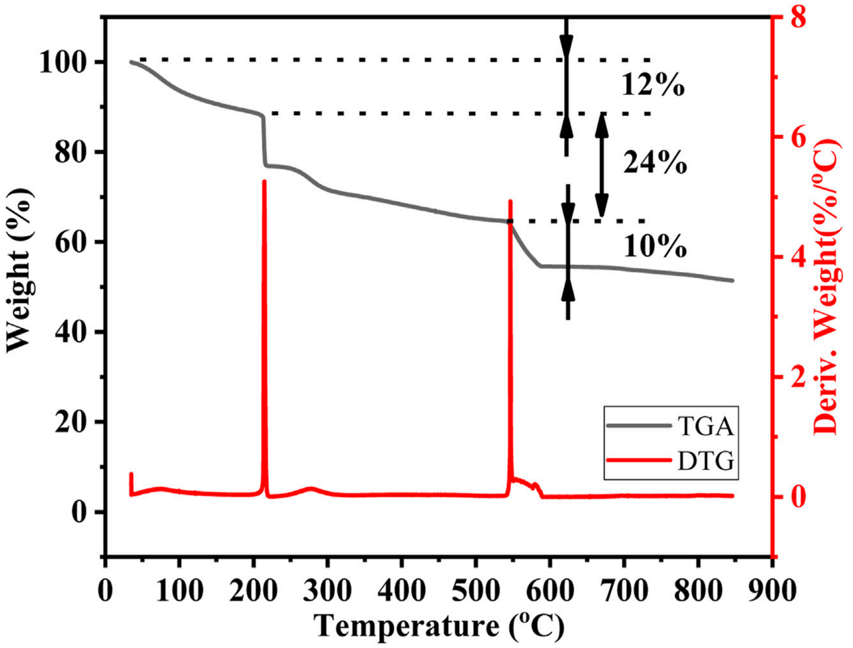

FIGURE 2
Thermogravimetric analysis (TGA) and derivative thermogravimetric (DTG) curves of the NCM523 precursor solution.

1–2 $mg\,cm^{-2}$. 1 M Potassium hydroxide (KOH) was used as the electrolyte for the measurements.

The measurements were conducted using the three-electrode configuration (3EC) to study exclusively the electrochemical properties of the textile NCM523 and the two-electrode configuration (2EC) to evaluate the full-cell capacitor's performance. In the 3EC, the textile NCM523 or non-textile NCM523 was the working electrode, a platinum foil was used as the counter electrode, and Ag/AgCl was used as the reference electrode. For the 2EC, the full cell was assembled by hybridizing the cathode of NCM523 with the anode of activated carbon (AC).

Cyclic Voltammetry (CV), Galvanostatic Charge-Discharge (GCD), and Electrochemical Impedance (EIS) were performed at room temperature using the CHI 660E electrochemical workstation. The voltage window was −0.1–0.5 V for the half-cell cathode, and −0.8 to 0.1 V for the anode, and different voltage windows were applied for the full cell (0–0.9 V, 0–1 V, 0–1.1 V, and 0–1.2 V). The stability was tested using GCD for 200 cycles. The specific discharge capacitance (C, $mhA\,g^{-1}$), charge balance, energy density (E, $Wh\,kg^{-1}$), and power density (P, $W\,kg^{-1}$) were calculated using the following equations (Eqs 1–4):

$$C = \frac{\int IdV}{vm\Delta V} = \frac{j\Delta t}{\Delta V} \tag{1}$$

Where I (A) is the response current, ν ($V\ s^{-1}$) is the scan rate, m is the mass loading of the NCM 523 and textile NCM523, ΔV (V) is the voltage window, j ($A\ mg^{-1}$) is the current density and Δt (s) is the discharging time.

$$\frac{m_+}{m_-} = \frac{C_{electrode-} \times \Delta E_-}{C_{electrode+} \times \Delta E_+} \tag{2}$$

Here, $m_\pm$ and $C_\pm$ represent the active material mass and specific capacitance of the positive (or negative) electrode, respectively, $\Delta E_\pm$ is the potential window of the positive (or negative) electrode.

$$E = \frac{1}{2} C\Delta V^2 \tag{3}$$

Where C is specific capacitance, ΔV (V) is the voltage window.

$$P = \frac{E}{\Delta t} \tag{4}$$

Here, E is energy density and Δt is the discharge time (s).

3 Results and discussion

3.1 Material characterization

To investigate processes during calcination, thermogravimetric analysis (TGA) and derivative thermogravimetric (DTG) analysis were conducted. The TGA was performed in a range between room temperature and 900°C at a rate of 10°C min^{-1} under air atmosphere subsuming a 3-step weight loss. As shown in Figure 2, the first step is mainly attributed to the desorption of water molecules which constituted 12 wt% between 25°C and 200°C. Then, the second step making up 24 wt% takes place from 200°C to 550°C including a sharp drop at 200°C accounting for the decomposition of the EDTA and PEI, followed by a gradual decline associated with the decomposition of the cellulose and polyester chains in the textiles. This sudden weight losses at corresponding temperature at 214°C in the DTG curve. The final loss is ascribed to the melting process of lithium from 550°C to 600°C, corresponding the peak at 546°C in DTG curve and the formation of the single-layered

TABLE 1 The relative contents of Li, Ni, Co, and Mn in NCM523 samples.

NCM523	Li	Ni	Co	Mn
Textile	1.01	0.48	0.20	0.31
Non-textile	1.05	0.43	0.20	0.30

hexagonal crystal structure of NCM523 after 700℃. To confirm the exact composition of prepared samples, elemental analysis was examined by ICP. Results are listed in Table 1, which is close to the targeted composition for NCM523 by heating at high temperature and controlling the amount of lithium precursor. Excess lithium may form amorphous Li_2CO_3 and LiOH, resulting in a decreased lithium ratio, while the slight loss of Ni in NCM523 might also be attributed to high-temperature evaporation.

The crystallinity and phase purity can be examined by the X-ray diffraction (XRD) patterns. Figure 3A compares the XRD patterns among the textile and non-textile NCM523 with the standard single-layered hexagonal crystal structure of lithium cobalt oxide ($LiCoO_2$). All the peak positions are almost aligned with the standard pattern despite a slight left shift because the dopants of Ni and Mn induces an expansion in lattice parameters of the crystal structure. The lattice parameters are tabulated in Table 2. The splitting of (108/110) and (006/102) peaks indicates a highly ordered hexagonal crystal structure (Xu et al., 2015; Meng et al., 2017). The integrated intensity ratio of the (003) and (104) are >1.4, indicating the suppressed cation mixing (Xu et al., 2015; Yabuuchi et al., 2011; Yang et al., 2014). The BET surface area was obtained by the isotherm curves as shown in Figure 3B. The textile NCM523 attains the surface area of 5.3 $m^2 g^{-1}$ while that of the non-textile NCM523 is as low as 1.3 $m^2 g^{-1}$. The difference proves that the textile template improves the surface area substantially.

The 3D structure is revealed in the SEM images. As shown in Figure 4A, the NCM523 material replicates the shape of the textiles forming a 3D interwoven network whereas the control sample fails to construct any specific shape. The particle distribution is also more even compared to that of the non-textile NCM523, as shown in Figures 4B–D. In addition, non-textile NCM523 presents some large particles attributing to the lower surface area.

3.2 Electrochemical measurements

3.2.1 Half-cell capacitor (3EC)

To further investigate the electrochemical behavior of the active materials, the relevant tests were carried out including CV, GCD, and EIS in the 1 M KOH three-electrode systems at room temperature. Figure 5A compares the CVs of both samples at a scan rate of 1 $mV\ s^{-1}$, where the area under the curve is entitled to the specific capacitance. Obvious strong redox peaks appear in curves of all electrodes, indicating that the pairs of redox peaks reveal the characteristics of pseudocapacitance (Eqs 5, 6) (Peng et al., 2015; Du et al., 2018):

$$Li\,(Ni_{0.5}Co_{0.2}Mn_{0.3})O_2 \rightarrow xLi^{+} + Li_{1-x}\,(Ni_{0.5}Co_{0.2}Mn_{0.3})O_2 \quad (5)$$

$$Li_{1-x}\,(Ni_{0.5}Co_{0.2}Mn_{0.3})O_2 + \frac{(1-x)}{2}OH^{-} \rightarrow 0.5NiOOH + 0.2MnOOH + 0.3CoOOH + \frac{(1-x)}{2}Li_2O + \frac{(1-x)}{2}e^{-} \quad (6)$$

Textile NCM523 electrode exhibited larger CV integrated areas than that of the non-NCM 523 electrode, indicating the introduction of 3D structure can improve the charge storage capacity of the

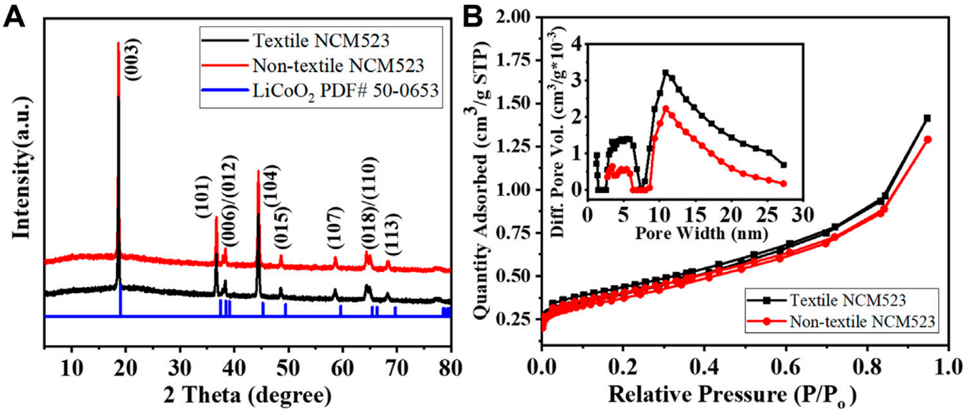

FIGURE 3
(A) XRD patterns of the NCM523 samples and the standard $LiCoO_2$; and **(B)** N_2 adsorption and desorption isotherm curves, inserted for pore size distribution.

TABLE 2 Computed XRD lattice parameters and surface area of NCM523 samples.

NCM523	a (Å)	c (Å)	c/a	I_{003}/I_{104}	BET surface area ($m^2 g^{-1}$)
Textile	2.8696	14.2628	4.9702	2.144	5.3
Non-textile	2.8676	14.2628	4.9738	2.111	1.3

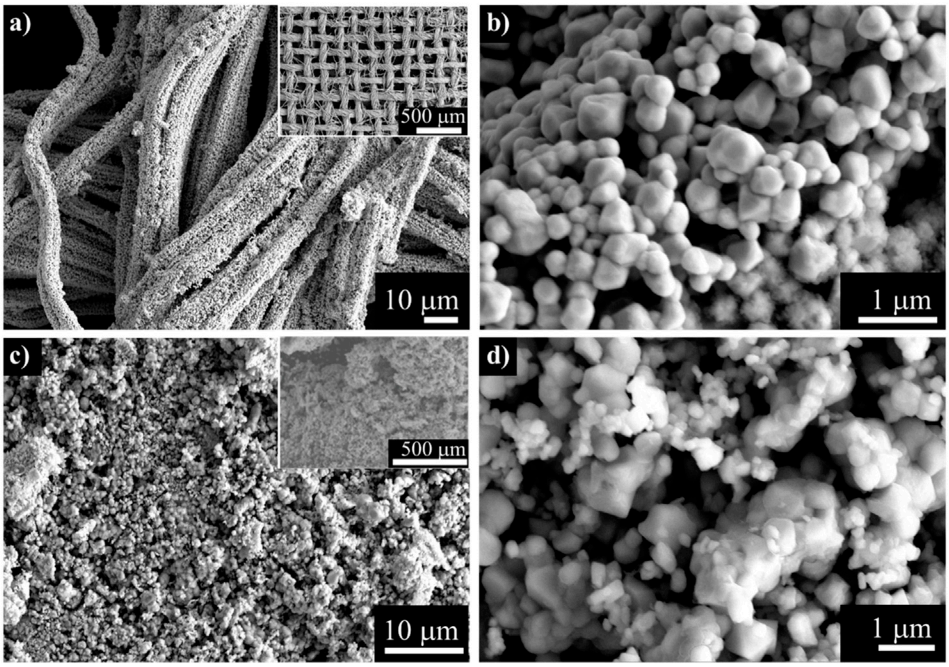

FIGURE 4
SEM images of **(A,B)** textile NCM523 and **(C,D)** non-textile NCM523.

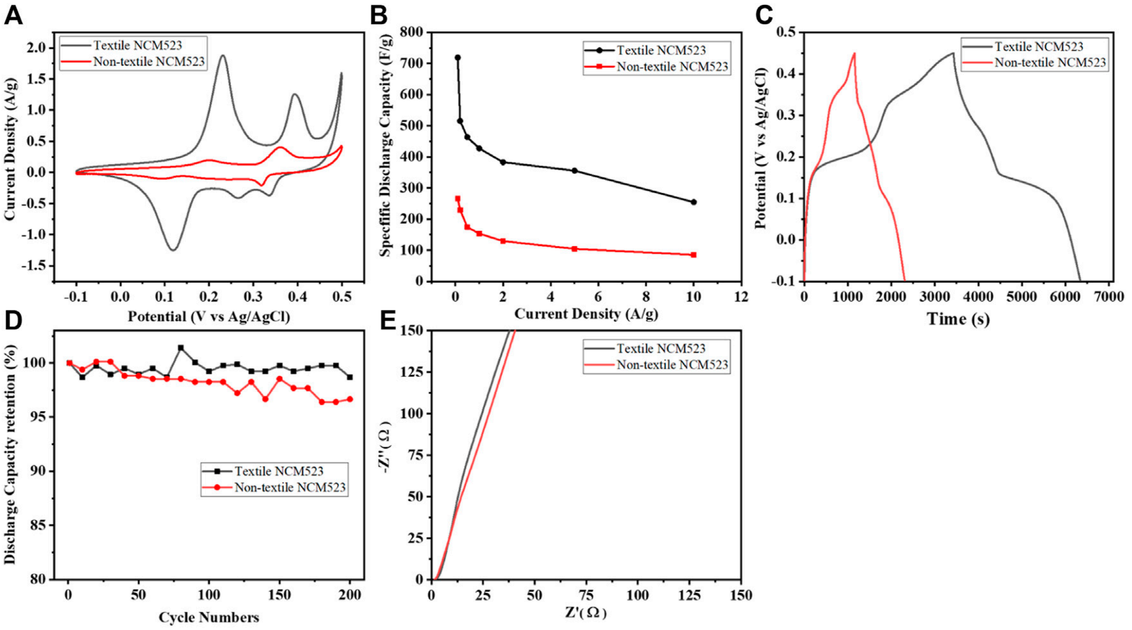

FIGURE 5
Electrochemical measurement results: **(A)** CV profile at the scan rate of 1 $mV\,s^{-1}$; **(B)** Capacitance at various current densities; **(C)** GCD profile at a current density of 1 $A\,g^{-1}$; and **(D)** Stability test using GCDs for 200 cycles; and **(E)** EIS of textile and non-textile NCM523.

electrode materials. GCDs were conducted at various current densities (0.1, 0.2, 0.5, 1, 2, 5, and 10 $A\,g^{-1}$) to calculate the specific discharge capacitance as shown in Figure 5B. The computed results are listed in Table 3. The capacitance of the textile NCM523 is maintained around 3 times larger than that of the non-textile NCM523. A comparison of GCD profiles for non-textile and textile NCM523 is shown in Figure 5C and GCD tests can be implemented in a potential window of –0.1 to 0.45 V (vs. Ag/AgCl) at a current density of 1 $A\,g^{-1}$. The nonlinear GCD curve of textile NCM523 electrode displays a similar charging/discharging time almost without obvious IR drops, indicating that the 3D structure electrode had high Coulombic efficiency and electrical

TABLE 3 Specific capacitance of textile and non-textile NCM523 at different current densities.

	Specific capacitance ($F\,g^{-1}$)	
Current density ($A\,g^{-1}$)	Textile NCM523	Non-textile NCM523
0.1	718.67	265.97
0.2	515.14	229.36
0.5	463.40	174.69
1	427.18	153.53
2	380.69	129.42
5	355.71	104.59
10	254.48	85.40

conductivity. This can be attributed to the 3D structure of the electrode as well as the good interfacial contact between NCM523 and the current collector. As expected, both capacitors employing NCM523 as the active material are quite stable after 200 cycles (Figure 5D). However, the one without textiles is slightly fading while the textile NCM523 remains at the retention rate of 100%. Finally, Figure 5E illustrates the Nyquist plots of non-textile and textile NCM523 over frequency range from 100 kHz to 0.1 Hz with an AC amplitude of 20 mV. It is worth noting that both figures show a similar appearance with no obvious semicircle in the high frequency region, indicating the significantly low charge transfer resistance (Rct) caused by the high-rate charge transfer process and fast electrode kinetic. Additionally, the slope of the line section at low frequency region is related to the diffusion rate of electrolyte ions within electrode. Therefore, the steeper slope for the textile NCM523 indicates that 3D structure facilitates rapid ion diffusion ability.

3.2.2 Full-cell capacitor (2EC)

AC with a mass load of 1 $mg\,cm^{-2}$ was prepared and tested in the 2EC as a working electrode under the same procedure to determine its capacitance. Then, Eq. 2 is used to monitor the

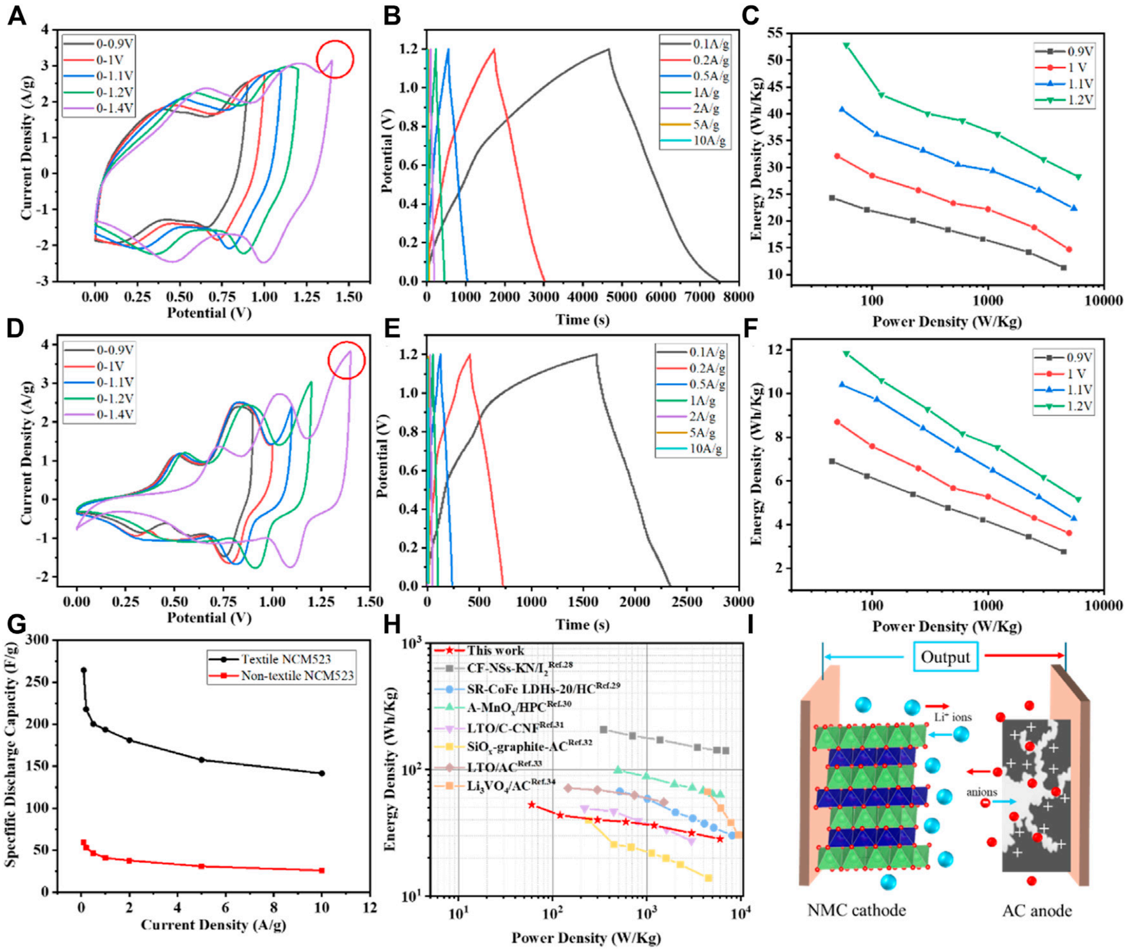

FIGURE 6
Electrochemical measurement results: **(A)** CV profiles at different voltage windows of the textile NCM523; **(B)** GCD profiles at different current densities of the textile NCM523; **(C)** Ragone plot of the textile NCM523; **(D)** CV profiles at different voltage windows of the non-textile NCM523; **(E)** GCD profiles at different current densities of the non-textile NCM523; **(F)** Ragone plot of the non-textile NCM523; **(G)** Capacitance at difference current densities for textile and non-textile NCM523; and **(H)** Ragone plot with the performance of the textile NCM523 edited from literature (Xu et al., 2014; Shen et al., 2017; Li et al., 2019a; Li et al., 2019b; Babu et al., 2020; Sun et al., 2023; Wang et al., 2023; Wang et al., 2024); **(I)** Schematic diagram of LIC using NMC cathode and AC anode.

incremental mass until the charge is balanced on both electrodes. In the electrochemical measurements of the full-cell capacitor, the testing procedures were similar except that CVs were operated at incremental voltage windows to find the energy density from Eq. 3. Figure 6A investigates the CV curve of textile NCM523 LIC under different potential windows at 10 mV s^{-1}. It can be confirmed that the CV curve has redox peaks on rectangular shape in the minimum potential range of 0–0.9 V and the maximum potential range of 0–1.4 V. Considering that the occurrence of oxygen evolution reaction (OER) with a strong and sharp peak at high potential range, most of the capacity contribution of NCM523 active material is within the potential window of 0–0.45 V (vs. Ag/AgCl). The operating voltage range is set at 0–1.2 V to avoid the risk of electrolyte concentration changes by OER reaction and the reduction of reversible capacity due to polarization. However, in Figure 6D for non-textile NCM523 LIC at potential range of 0–1.2 V, the sharp OER peak almost dominates the profile. Consequently, the voltage range of 0–1.2 V is not suitable for non-textile NCM523 and this potential is considered harmful to the reversibility of the redox reactions in the control sample due to the intense behavior of OER. Thus, The CV curves under different scanning rates maintain a good shape and reversibility, which proves that the textile NCM523 with 3D structure achieved satisfactory electrochemical performances. The GCD performance of the non-textile and textile NCM523 LICs recorded at different current densities from 0.1 to 10 A g^{-1} are plotted in Figures 6B, E and the nonlinear charge-discharge profile curves further confirm the characteristic feature of pseudocapacitive behavior. Based on the GCD curve discharge time, the capacitance of non-textile and textile NCM523 LICs performance was calculated using Eq. 1 and shows in Figure 6G Being consistent with the findings in the half-cell capacitor measurements, the capacitance for the NCM523 with the 3D architecture is also more than three-fold higher than that of the non-textile sample. More importantly, the Ragone plots shown in Figures 6C, F prove a synergistic effect of the 3D structure on the energy density, where the capacitor can attain up to 36.17 $Wh\,kg^{-1}$ at the power density of 1,200 $W\,kg^{-1}$ and voltage window of 0–1.2 V. Moreover, the energy density only slightly decreases to 28.26 $Wh\,kg^{-1}$ as the power density is increased to 6,000 $W\,kg^{-1}$. In contrast, even at the power density as low as 60 $W\,kg^{-1}$, the non-textile's energy density is 11.83 $Wh\,kg^{-1}$, which is too inferior to the textile NCM523. At the maximum power density of 6,000 $W\,kg^{-1}$, the energy density of the non-textile NCM523 shrinks to only 5.17 $Wh\,kg^{-1}$. This result is considered significant when comparing the textile NCM523 performances with the existing LICs in Figure 6H, the energy densities at the lower power density points of 3,000 and 6,000 $W\,kg^{-1}$ are noticeably superior making LICs one step closer to the ideal performances of the combustion engines. The improvement is ascribed to the 3D integrity allowing larger surface area supporting the ion-exchange process at high reaction rates. The LICs were composed of the NMC cathode and activated carbon (AC) anode, as shown in Figure 6I. During charging, Li ions are intercalated in the Li-ion materials and anions are adsorbed on the surface of AC electrode.

4 Conclusion

The 3D NCM523 was successfully synthesized with suppressed cation mixing and facilitated the ion exchange process at the interface. In addition, the incorporation of 3D integrity allows to reach a higher capacitance for the half-cell capacitor while improving the energy density of the full-cell capacitor. Not only is the electrochemical performance dominant over the non-textile NCM523, but it also surpasses the existing LIC's materials making it a promising choice for ultra-performance energy storage devices.

Data availability statement

The raw data supporting the conclusion of this article will be made available by the authors, without undue reservation.

Author contributions

PT: Writing–original draft, Methodology, Data curation. QS: Writing–original draft, Methodology, Investigation, Formal Analysis, Data curation. WT: Writing–review and editing, Validation, Investigation, Formal Analysis. RH: Writing–review and editing, Validation, Methodology, Investigation, Formal Analysis. MZ: Writing–review and editing, Writing–original draft, Validation, Supervision, Resources, Project administration, Methodology, Investigation, Funding acquisition, Formal Analysis, Conceptualization. HL: Writing–review and editing, Validation, Supervision, Resources, Project administration, Methodology, Investigation, Conceptualization.

Funding

The author(s) declare that financial support was received for the research, authorship, and/or publication of this article. The work is supported by the U.S. National Science Foundation OIA-2119688.

Conflict of interest

The authors declare that the research was conducted in the absence of any commercial or financial relationships that could be construed as a potential conflict of interest.

Publisher's note

References

Amatucci, G. G., Badway, F., Du Pasquier, A., and Zheng, T. (2001). An asymmetric hybrid nonaqueous energy storage cell. *J. Electrochem. Soc.* 148 (8), A930. doi:10.1149/1.1383553

Babu, B., Simon, P., and Balducci, A. (2020). Fast charging materials for high power applications. *Adv. Energy Mater.* 10 (29), 2001128. doi:10.1002/aenm.202001128

Chen, S., Hu, H., Wang, C., Wang, G., Yin, J., and Cao, D. (2012). $LiFePO_4$-AC/$Li_4Ti_5O_{12}$ hybrid supercapacitor: the effect of $LiFePO_4$ content on its performance. *J. Renew. Sustain. Energy* 4 (3), 033114. doi:10.1063/1.4727929

Du, H., Li, Y., Ding, F., Zhao, J., Zhang, X., Li, Y., et al. (2018). Boosting the capacitance of NiCo2O4 hierarchical structures on nickel foam in supercapacitors. *Int. J. Hydrogen Energy* 43 (32), 15348–15357. doi:10.1016/j.ijhydene.2018.06.079

Education, E. (2018). Energy density vs power density. Available at: https://energyeducation.ca/encyclopedia/Energy_density_vs_power_density.

engineering (2017). Case school of engineering, C. W. R. U. Electrochemical devices. Available at: https://engineering.case.edu/chemical-and-biomolecular-engineering/research/electrochemical-devices.

Gnanomat (2019). Gnanomat innovative energy storage systems. Available at: https://gnanomat.com/2019/05/16/innovative-energy-storage-systems/.

Hagen, M., Cao, W., Shellikeri, A., Adams, D., Chen, X., Brandt, W., et al. (2018). Improving the specific energy of Li-Ion capacitor laminate cell using hybrid activated Carbon/LiNi0. 5Co0. 2Mn0. 3O2 as positive electrodes. *J. Power Sources* 379, 212–218. doi:10.1016/j.jpowsour.2018.01.036

Kötz, R., and Carlen, M. (2000). Principles and applications of electrochemical capacitors. *Electrochimica acta* 45 (15-16), 2483–2498. doi:10.1016/s0013-4686(00)00354-6

Kuwata, N., Lu, X., Miyazaki, T., Iwai, Y., Tanabe, T., and Kawamura, J. (2016). Lithium diffusion coefficient in amorphous lithium phosphate thin films measured by secondary ion mass spectroscopy with isotope exchange methods. *Solid State Ionics* 294, 59–66. doi:10.1016/j.ssi.2016.06.015

Lee, S.-H., and Im, I.-H. (2018). Excellent performance hybrid supercapacitors based on $LiNi_{1/3}Mn_{1/3}Co_{1/3}O_2$/activated carbon electrode. *Mater. Lett.* 231, 38–42. doi:10.1016/j.matlet.2018.07.115

Lewandowski, A., and Galinski, M. (2007). Practical and theoretical limits for electrochemical double-layer capacitors. *J. Power Sources* 173 (2), 822–828. doi:10.1016/j.jpowsour.2007.05.062

Li, C., Zhang, X., Wang, K., Sun, X., and Ma, Y. (2019a). A 29.3 Wh kg– 1 and 6 kW kg– 1 pouch-type lithium-ion capacitor based on SiOx/graphite composite anode. *J. Power Sources* 414, 293–301. doi:10.1016/j.jpowsour.2018.12.090

Li, H., Guo, S., Wang, L., Wu, J., Zhu, Y. J., and Hu, X. (2019b). Thermally durable lithium-ion capacitors with high energy density from all hydroxyapatite nanowire-enabled fire-resistant electrodes and separators. *Adv. Energy Mater.* 9 (46), 1902497. doi:10.1002/aenm.201902497

Meng, K., Wang, Z., Guo, H., and Li, X. (2017). Enhanced cycling stability of $LiNi_{0.8}Co_{0.1}Mn_{0.1}O_2$ by reducing surface oxygen defects. *Electrochimica Acta* 234, 99–107. doi:10.1016/j.electacta.2017.03.054

Muto, S., Sasano, Y., Tatsumi, K., Sasaki, T., Horibuchi, K., Takeuchi, Y., et al. (2009). Capacity-fading mechanisms of $LiNiO_2$-based lithium-ion batteries: II. diagnostic analysis by electron microscopy and spectroscopy. *J. Electrochem. Soc.* 156 (5), A371. doi:10.1149/1.3076137

Peng, L., Zhu, Y., Khakoo, U., Chen, D., and Yu, G. (2015). Self-assembled LiNi1/3Co1/3Mn1/3O2 nanosheet cathodes with tunable rate capability. *Nano Energy* 17, 36–42. doi:10.1016/j.nanoen.2015.07.031

Sedajová, V., Jakubec, P., Bakandritsos, A., Ranc, V., and Otyepka, M. (2020). New limits for stability of supercapacitor electrode material based on graphene derivative. *Nanomaterials* 10 (9), 1731. doi:10.3390/nano10091731

Sharma, P., and Bhatti, T. (2010). A review on electrochemical double-layer capacitors. *Energy Convers. Manag.* 51 (12), 2901–2912. doi:10.1016/j.enconman.2010.06.031

Shen, L., Lv, H., Chen, S., Kopold, P., van Aken, P. A., Wu, X., et al. (2017). Peapod-like Li3VO4/N-doped carbon nanowires with pseudocapacitive properties as advanced materials for high-energy lithium-ion capacitors. *Adv. Mater.* 29 (27), 1700142. doi:10.1002/adma.201700142

Su, X., Yu, L., Cheng, G., Zhang, H., Sun, M., and Zhang, X. (2015). High-performance α-MnO2 nanowire electrode for supercapacitors. *Appl. Energy* 153, 94–100. doi:10.1016/j.apenergy.2014.07.094

Sun, Z., Han, X., and Wang, D. (2023). Zinc-iodine battery-capacitor hybrid device with excellent electrochemical performance enabled by a robust iodine host. *J. Energy Storage* 62, 106857. doi:10.1016/j.est.2023.106857

Supply, E. (2021). Energy supply evolves to meet demand projections. Available at: https://corporate.exxonmobil.com/Energy-and-innovation/Outlook-for-Energy/Energy-supply#Naturalgas.

Vlad, A., Singh, N., Rolland, J., Melinte, S., Ajayan, P., and Gohy, J.-F. (2014). Hybrid supercapacitor-battery materials for fast electrochemical charge storage. *Sci. Rep.* 4 (1), 4315–4317. doi:10.1038/srep04315

Wang, D., Han, X., and Zhang, X. (2024). Achieving high-capacity aqueous calcium-ion storage in amorphous manganese oxide nanospheres for calcium-ion asymmetric supercapacitors. *J. Power Sources* 599, 234215. doi:10.1016/j.jpowsour.2024.234215

Wang, D., Sun, J., and Chen, L. (2023). Structural reconstruction strategy enables CoFe LDHs for high-capacity NH4+ storage and application in high-energy density ammonium-ion hybrid supercapacitors. *ChemSusChem* 16 (12), e202300207. doi:10.1002/cssc.202300207

Xu, H., Hu, X., Sun, Y., Luo, W., Chen, C., Liu, Y., et al. (2014). Highly porous Li4Ti5O12/C nanofibers for ultrafast electrochemical energy storage. *Nano Energy* 10, 163–171. doi:10.1016/j.nanoen.2014.09.003

Xu, M., Chen, Z., Zhu, H., Yan, X., Li, L., and Zhao, Q. (2015). Mitigating capacity fade by constructing highly ordered mesoporous Al_2O_3/polyacene double-shelled architecture in Li-rich cathode materials. *J. Mater. Chem. A* 3 (26), 13933–13945. doi:10.1039/c5ta03676c

Yabuuchi, N., Yoshii, K., Myung, S.-T., Nakai, I., and Komaba, S. (2011). Detailed studies of a high-capacity electrode material for rechargeable batteries, Li_2MnO_3–$LiCo_{1/3}N_{i1/3}Mn_{1/3}O_2$. *J. Am. Chem. Soc.* 133 (12), 4404–4419. doi:10.1021/ja108588y

Yang, X., Wang, D., Yu, R., Bai, Y., Shu, H., Ge, L., et al. (2014). Suppressed capacity/voltage fading of high-capacity lithium-rich layered materials via the design of heterogeneous distribution in the composition. *J. Mater. Chem. A* 2 (11), 3899–3911. doi:10.1039/c3ta14513a

Yuan, C., Lin, H., Lu, H., Xing, E., Zhang, Y., and Xie, B. (2016). Synthesis of hierarchically porous MnO_2/rice husks derived carbon composite as high-performance electrode material for supercapacitors. *Appl. Energy* 178, 260–268. doi:10.1016/j.apenergy.2016.06.057

Zhao, D., and Li, S. (2020). Regulating the performance of lithium-ion battery focus on the electrode-electrolyte interface. *Front. Chem.* 8, 821. doi:10.3389/fchem.2020.00821

Zhao, L., Chen, G., Weng, Y., Yan, T., Shi, L., An, Z., et al. (2020). Precise Al_2O_3 coating on $LiNi_{0.5}Co_{0.2}Mn_{0.3}O_2$ by atomic layer deposition restrains the shuttle effect of transition metals in Li-ion capacitors. *Chem. Eng. J.* 401, 126138. doi:10.1016/j.cej.2020.126138